Cross-correlation-based image acquisition technique for manually-scanned optical coherence tomography

Adeel Ahmad[1], Steven G. Adie[1], Eric J. Chaney[1], Utkarsh Sharma[1], and Stephen A. Boppart*[1, 2]

Biophotonics Imaging Laboratory
Beckman Institute for Advanced Science and Technology
[1] Department of Electrical and Computer Engineering,
[2] Department of Bioengineering, Department of Medicine
University of Illinois at Urbana-Champaign
405 N. Mathews Avenue, Urbana, IL 61801
[*]Corresponding author: boppart@illinois.edu

Abstract: We present a novel image acquisition technique for Optical Coherence Tomography (OCT) that enables manual lateral scanning. The technique compensates for the variability in lateral scan velocity based on feedback obtained from correlation between consecutive A-scans. Results obtained from phantom samples and biological tissues demonstrate successful assembly of OCT images from manually-scanned datasets despite non-uniform scan velocity and abrupt stops encountered during data acquisition. This technique could enable the acquisition of images during manual OCT needle-guided biopsy or catheter-based imaging, and for assembly of large field-of-view images with hand-held probes during intraoperative *in vivo* OCT imaging.

OCIS codes: (170.4500) Optical coherence tomography; (120.5800) Scanners

References and links

1. D. Huang, E. A. Swanson, C. P. Lin, J. S. Schuman, W. G. Stinson, W. Chang, M. R. Hee, T. Flotte, K. Gregory, C. A. Puliafito, and J. G. Fujimoto, "Optical coherence tomography," Science **254**, 1178-1181 (1991).
2. W. Drexler, and J. G. Fujimoto, *Optical coherence tomography: technology and applications* (Springer, New York 2008).
3. A. M. Zysk, F. T. Nguyen, A. L. Oldenburg, D. L. Marks, and S. A. Boppart, "Optical coherence tomography: a review of clinical development from bench to bedside," J. Biomed. Opt **12**, 051403-051421 (2007).
4. R. Huber, M. Wojtkowski, and J. G. Fujimoto, "Fourier domain mode locking (FDML): A new laser operating regime and applications for optical coherence tomography," Opt. Express **14**, 3225-3237 (2006).
5. Z. Chen, Z. Yonghua, S. M. Srinivas, J. S. Nelson, N. Prakash, and R. D. Frostig, "Optical Doppler tomography," IEEE J. Sel. Top. Quantum Electron. **5**, 1134-1142 (1999).
6. J. J. Pasquesi, S. C. Schlachter, M. D. Boppart, E. J. Chaney, S. J. Kaufman, and S. A. Boppart, "*In vivo* detection of exercise-induced ultrastructural changes in genetically-altered murine skeletal muscle using polarization-sensitive optical coherence tomography," Opt. Express **14**, 1547-1556 (2006).
7. A. L. Oldenburg, V. Crecea, S. A. Rinne, and S. A. Boppart, "Phase-resolved magnetomotive OCT for imaging nanomolar concentrations of magnetic nanoparticles in tissues," Opt. Express **16**, 11525-11539 (2008).
8. S. A. Boppart, W. Luo, D. L. Marks, and K. W. Singletary, "Optical coherence tomography: feasibility for basic research and image-guided surgery of breast cancer," Breast Cancer Res. Treatment **84**, 85-97 (2004).
9. S. Radhakrishnan, A. M. Rollins, J. E. Roth, S. Yazdanfar, V. Westphal, D. S. Bardenstein, and J. A. Izatt, "Real-time optical coherence tomography of the anterior segment at 1310 nm," Arch. Ophthalmol. **119**, 1179-1185 (2001).
10. F. I. Feldchtein, V. M. Gelikonov, and G. V. Gelikonov, *"Design of OCT scanners" in Handbook of optical coherence tomography* (Marcel Dekker, Inc, 2002).

11. X. Li, C. Chudoba, T. Ko, C. Pitris, and J. G. Fujimoto, "Imaging needle for optical coherence tomography," Opt. Lett. **25**, 1520-1522 (2000).
12. S. A. Boppart, B. E. Bouma, C. Pitris, G. J. Tearney, J. G. Fujimoto, and M. E. Brezinski, "Forward-imaging instruments for optical coherence tomography," Opt. Lett. **22**, 1618-1620 (1997).
13. S. Han, M. V. Sarunic, J. Wu, M. Humayun, and C. Yang, "Handheld forward-imaging needle endoscope for ophthalmic optical coherence tomography inspection," J. Biomed. Opt **13**, 020505 (2008).
14. P. Cinquin, E. Bainville, C. Barbe, E. Bittar, V. Bouchard, I. Bricault, G. Champleboux, M. Chenin, L. Chevalier, Y. Delnondedieu, L. Desbat, V. Dessenne, A. Hamadeh, D. Henry, N. Laieb, S. Lavallee, J. M. Lefebvre, F. Leitner, Y. Menguy, F. Padieu, O. Peria, A. Poyet, M. Promayon, S. Rouault, P. Sautot, J. Troccaz, and P. Vassal, "Computer assisted medical interventions," IEEE. Eng. Med. Biol. Mag **14**, 254-263 (1995).
15. R. L. Galloway, "The process and development of image guided procedures," Annu. Rev. Biomed. Eng **3**, 83-108 (2001).
16. A. H. Gee, R. James Housden, P. Hassenpflug, G. M. Treece, and R. W. Prager, "Sensorless freehand 3D ultrasound in real tissue: Speckle decorrelation without fully developed speckle," Med. Image Anal **10**, 137-149 (2006).
17. L. Mercier, T. Langø, F. Lindseth, and D. L. Collins, "A review of calibration techniques for freehand 3-D ultrasound systems," Ultrasound Med. Biol **31**, 449-471 (2005).
18. P. Hassenpflug, R. W. Prager, G. M. Treece, and A. H. Gee, "Speckle classification for sensorless freehand 3-D ultrasound," Ultrasound Med. Biol **31**, 1499-1508 (2005).
19. T. A Tuthill, J. F. Krucker, J. B. Fowlkes, and P. L. Carson, "Automated three-dimensional US frame positioning computed from elevational speckle decorrelation," Radiology **209**, 575-582 (1998).
20. L. Pai-Chi, C. Chong-Jing, and Y. Chih-Kuang, "On velocity estimation using speckle decorrelation " IEEE. Trans. Ultrason. Ferroelectr. Freq. Control **48**, 1084-1091 (2001).
21. R. W. Prager, A. H. Gee, G. M. Treece, C. J. C. Cash, and L. H. Berman, "Sensorless freehand 3-D ultrasound using regression of the echo intensity," Ultrasound Med. Biol **29**, 437-446 (2003).
22. A. Krupa, G. Fichtinger, and G. D. Hager, "Full Motion Tracking in Ultrasound Using Image Speckle Information and Visual Servoing," in *Proceedings of IEEE International Conference on Robotics and Automation* (2007), pp. 2458-2464.
23. P. C. Li, C. Y. Li, and W. C. Yeh, "Tissue motion and elevational speckle decorrelation in freehand 3D ultrasound," Ultrason. Imaging **24**, 1-12 (2002).
24. K. W. Gossage, T. S. Tkaczyk, J. J. Rodriguez, and J. K. Barton, "Texture analysis of optical coherence tomography images: feasibility for tissue classification," J. Biomed. Opt **8**, 570-575 (2003).
25. S. J. Kirkpatrick, R. K. Wang, and D. D. Duncan, "OCT-based elastography for large and small deformations," Opt. Express **14**, 11585-11597 (2006).
26. D. D. Duncan, and S. J. Kirkpatrick, "Processing algorithms for tracking speckle shifts in optical elastography of biological tissues," J. Biomed. Opt **6**, 418-426 (2001).
27. D. D. Duncan, and S. J. Kirkpatrick, "Performance analysis of a maximum-likelihood speckle motion estimator," Opt. Express **10**, 927-941 (2002).
28. H.-J. Ko, W. Tan, R. Stack, and S. A. Boppart, "Optical coherence elastography of engineered and developing tissue," Tissue Eng **12**, 63-73 (2006).
29. S. H. Yun, G. J. Tearney, J. F. de Boer, and B. E. Bouma, "Motion artifacts in optical coherence tomography with frequency-domain ranging," Opt. Express **12**, 2977-2998 (2004).
30. R. J. Zawadzki, S. S. Choi, S. M. Jones, S. S. Oliver, and J. S. Werner, "Adaptive optics-optical coherence tomography: optimizing visualization of microscopic retinal structures in three dimensions," J. Opt. Soc. Am. A **24**, 1373-1383 (2007).
31. J. M. Schmitt, S. H. Xiang, and K. M. Yung, "Speckle in optical coherence tomography," J. Biomed. Opt **4**, 95-105 (1999).
32. W. Luo, D. L. Marks, T. S. Ralston, and S. A. Boppart, "Three-dimensional optical coherence tomography of the embryonic murine cardiovascular system," J. Biomed. Opt **11**, 021014-021018 (2006).
33. A. M. Zysk, and S. A. Boppart, "Computational methods for analysis of human breast tumor tissue in optical coherence tomography images," J. Biomed. Opt **11**, 054015 (2006).
34. M. Wojtkowski, V. J. Srinivasan, T. H. Ko, J. G. Fujimoto, A. Kowalczyk, and J. S. Duker, "Ultrahigh-resolution, high-speed, fourier domain optical coherence tomography and methods for dispersion compensation," Opt. Express **12**, 2404-2422 (2004).
35. R. J. Housden, A. H. Gee, R. W. Prager, and G. M. Treece, "Rotational motion in sensorless freehand three-dimensional ultrasound," Ultrasonics **48**, 412-422 (2008).
36. R. J. Housden, A. H. Gee, G. M. Treece, and R. W. Prager, "Subsample interpolation strategies for sensorless freehand 3D ultrasound," Ultrasound Med. Biol **32**, 1897-1904 (2006).

1. Introduction

Optical coherence tomography (OCT) is a non-invasive optical imaging technique which measures backscattered light to provide high resolution (1-10µm) cross-sectional or three

dimensional images of biological tissues [1]. The OCT technology has undergone significant advances in instrumentation that has expanded its clinical applications [2, 3]. The development of Fourier-domain acquisition methods have made it possible to acquire real-time *in vivo* images with enhanced sensitivity and high scan rates [4], and various structural, functional and molecular contrast enhancing methods such as Doppler OCT, polarization-sensitive OCT, spectroscopic OCT, and magnetomotive OCT have further extended the range of possible applications of OCT [5-7].

One of the major advantages of OCT is that it provides real-time non-invasive diagnostic feedback about microscopic tissue architecture. This information, for example, is useful to physicians to assist them in making real-time decisions during time-sensitive diagnostic and surgical procedures such as needle biopsy, minimally-invasive surgery or procedures, or the removal of tumor tissue [8]. Despite the real-time, high-resolution imaging capabilities of OCT, the feasibility and success of implementing OCT in clinical and intraoperative conditions may largely be determined by the adaptability of OCT instrumentation and image acquisition techniques to make it more 'surgeon friendly'. While real-time portable OCT systems have been successfully demonstrated for clinical research over the last few years [9], the technology has yet to evolve towards providing an imaging capability that can be readily used by physicians under the diverse set of conditions encountered in an operating room.

Conventionally, in OCT imaging of tissue specimens or pre-clinical models, the specimen is placed on a fixed stage and an OCT image is acquired by sequential acquisition of depth-resolved A-scans synchronized with the lateral scanning of the beam using the computer-controlled motion of galvanometer-mounted mirrors. While this method provides excellent accuracy, the lateral scan range is limited by the limited angular range of the galvanometer and the finite aperture of the objective lens. Although using larger diameter objective lenses could enhance the scan range, they add to the bulk of the sample arm, which is even more problematic for hand-held mechanically-scanning probes. An alternative approach to obtain larger field-of-view is to keep the sample arm beam fixed and translate the sample at a uniform velocity using a stepper motor controlled stage. Clearly this method is impractical for *in vivo* OCT imaging applications, and the translation rate is slow. Various hand-held scanners and needle-based beam delivery systems have been reported which can provide more convenient access to tissues and organs in a clinical environment. Most of these scanners have a means for lateral scanning within the probe head [10-13]. However, these mechanisms make the probe more complicated, bulky, and expensive. Mechanical scanning mechanisms also frequently need to be customized for specific *in vivo* and intraoperative OCT imaging applications while still providing limited flexibility in choosing the scanning geometries. The added complexity and cost due to customized designs could make OCT a less attractive option for a number of applications.

In many circumstances, a surgeon might prefer to use a simple hand-held manually-scanned probe to obtain OCT images of tissues and organs which might otherwise be inaccessible using standard mechanically-scanning probes. However, manually scanning a hand-held probe can cause a number of image artifacts due to variations in the scan velocity and orientation of the probe. Consequently, image formation with a manually-scanning probe requires a method to synchronize the acquired A-scans with the relative displacement between the sample and probe. Methods similar to position tracking of surgical instruments in image-guided surgical systems can be used for this purpose [14]. These systems attach reference markers to the probe that are commonly sensed by optical or magnetic field sensors. The position of these reference markers is tracked by cameras or other suitable sensing systems, allowing compensation for the relative movement between the sample and the probe [15]. Despite their popularity, the use of an external position sensor is not ideal as it imposes a number of constraints on image acquisition. These sensors have to be carefully calibrated, typically have sub-millimeter spatial resolution, and the operating distances need to be within the range of the mounted sensor and the base unit. For sensors based on optics, a clear line of

sight must be maintained [16], while magnetic field-based sensing systems are highly susceptible to electromagnetic interference [17].

Clearly, position tracking without the use of an external position sensor can offer significant advantages. The challenge, however, is to utilize the acquired data or images to deduce precise motion estimation. Sensorless freehand scanning using speckle decorrelation has been extensively studied in ultrasound [18, 19]. Speckle decorrelation methods have been used in ultrasound for velocity estimation [20], 3-D ultrasound [21], and motion tracking [22] with varying success. One study reported that accurate displacement estimation in sensorless freehand ultrasound is not possible using speckle decorrelation methods alone [23]. In optics, speckle patterns have been used for image analysis [24] and elastography [25]. Motion artifact correction, tissue elastography, and blood velocity measurements in OCT all rely heavily on motion estimation techniques [25-29]. Algorithms based on 2-D cross-correlations of B-mode OCT images have been used in tissue elastography [25] and motion artifact correction [30].

In this paper we present a novel technique for the acquisition of manually-scanned OCT images based on the cross-correlation of A-scans within a 2-D OCT image. This method not only provides a simpler and less expensive scanning solution with an extended field-of-view, but also allows greater flexibility and freedom of movement while acquiring OCT images. The focus of this research study is to compensate for the image distortion and inaccuracies that occur during non-uniform motion of the probe during lateral manual scanning. To the best of our knowledge, no prior work has been done in applying motion estimation techniques for image formation in sensorless manual-scanning OCT. In Section 2 we present details of the cross-correlation algorithm used for image assembly. Section 3 presents typical decorrelation curves, followed by results of images assembled from manually-scanned tissue phantoms and biological tissues. We summarize the main findings and significance of this work in Section 4, followed by conclusions in Section 5.

2. Methods

2.1 Image acquisition algorithm

The algorithm used for image assembly is shown schematically in Fig. 1. An OCT image is a sequential assembly of uniformly spaced A-scans. Consecutive A-scans within one resolution volume will have high cross-correlation due to the regions of overlap, depending on the amount of oversampling of the sample. Oversampling in this context means sampling more than twice within the transverse resolution of the OCT system, which depends upon both the transverse resolution of the OCT system and the lateral step size. Due to the high A-scan rates available with current systems, and to fully reconstruct the features of the sample, OCT images are usually oversampled. We define the sampling factor ζ for a manually-scanned system as:

$$\zeta = \frac{f_s \Delta x}{v} \qquad (1)$$

where Δx is the transverse resolution of the OCT system which is equal to the diameter of the beam ($1/e^2$ intensity) at the focus in the sample arm, f_s is the A-scan acquisition rate (Hz) and v is the velocity of the moving sample or probe. A value of $\zeta < 2$ indicates undersampling and $\zeta > 2$ oversampling. Note that sampling at the Nyquist rate occurs when $\zeta = 2$.

Non-uniform movement of the probe will cause non-uniform sampling of the sample which in turn causes variability in the cross-correlation between adjacent A-scans. While slower scan velocities will result in sequential A-scans with higher correlation, faster scan velocities will result in reduced correlation between successive A-scans. The maximum velocity with which the probe or sample can move relative to each other to prevent undersampling is determined when $\zeta = 2$ in Eq. (1). The goal of the algorithm presented here is to discard all oversampled regions of a manually-scanned image, essentially reconstructing

the OCT image by assembling A-scans which are equally sampled in distance rather than equally sampled in time.
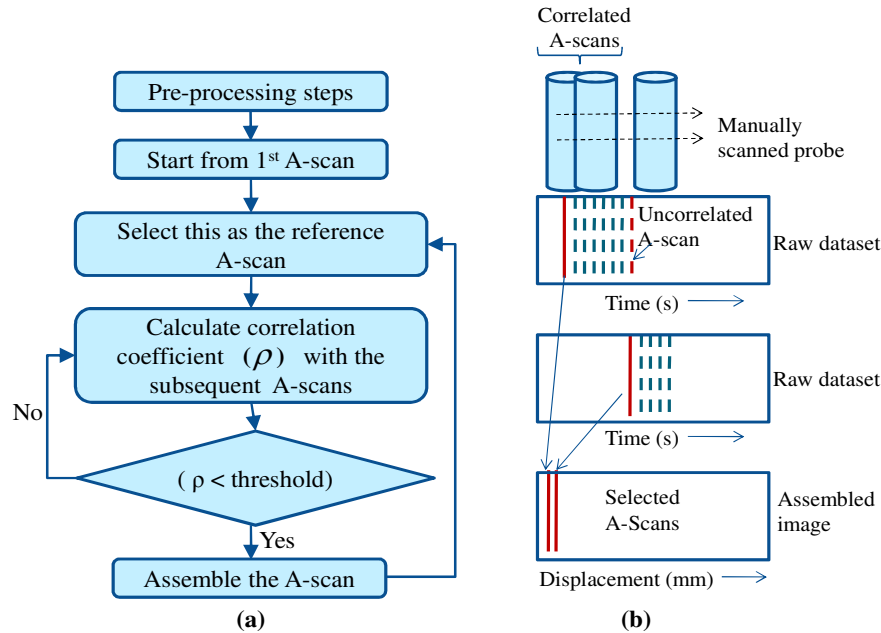

Fig. 1. (a) Flow chart representation of the algorithm. (b) The cross-correlation between A-scans decreases with the lateral displacement of the beam. The raw dataset contains A-scans uniformly placed in time, but due to non-uniform manual scanning, the successive A-scans have non-uniform displacement. The assembled image consists of A-scans selected by the algorithm which are uniformly spaced in distance.

The degree of correlation between A-scans can be measured by the Pearson cross-correlation coefficient given by

$$\rho(i, j) = \frac{< (I_i - \mu_i)(I_j - \mu_j) >}{\sigma_i \sigma_j} \qquad (2)$$

Where $< >$ is the expected value, I_i and I_j are the intensities of the sequential A-scans, and μ_i, μ_j and σ_i, σ_j are the means and standard deviations of the corresponding i^{th} and j^{th} A-scans. Identical A-scans would correspond to perfect correlation ($\rho = 1$) whereas highly uncorrelated A-scans exhibit zero or no correlation ($\rho = 0$). The cross-correlation between adjacent scans will depend not only upon the sample structure, but also on the sampling factor, speckle pattern [31], and the signal-to-noise ratio of the images.

Several pre-processing steps were performed prior to computing the cross-correlation coefficients. To make the algorithm more robust to variations in the sample structure and to increase the dependency on the speckle pattern from the sample, the output from a two-dimensional moving-average filter was subtracted from the raw image. Noise contributions were also minimized by truncating each A-scan so that only the portion containing sample information was selected. The size of the moving average (MA) filter should be of the order of several resolution elements (both in axial and lateral direction). Whereas a lower value of MA filter size will result in loss of useful speckle information, a higher value will make the decorrelation curves less sensitive to the slowly varying sample structure and attenuated signal in the axial direction. The size of the filter along the axial dimension was independent of the lateral scan velocity and was chosen to be around 5-6 times the axial resolution elements. The optimal choice of the filter dimension in the lateral direction will depend on the

lateral scanned velocity, however when used in conjunction with the axial dimension the choice of filter size along this direction is less critical.

A decorrelation curve plotted for a sample depicts the decrease in the correlation coefficient value as a function of lateral displacement between two A-scans. Based on the decorrelation curve of a sample, a threshold can be determined, corresponding to the desired sampling factor for the assembled image. The first A-scan is selected as the reference and the cross-correlation coefficients with the subsequently-acquired A-scans are computed. When the correlation coefficient falls below the selected threshold, the displacement is deemed to satisfy the desired sampling criteria, and the A-scan is appended to the assembled image. This assembled A-scan is now selected as the new reference and the steps are repeated until the algorithm iterated through all acquired A-scans.

2.2 Experimental setup

Measurements were conducted using the spectral-domain OCT system described previously [32]. Briefly, a Ti-Sapphire laser with 800 nm center wavelength and 90 nm bandwidth was used, providing an axial resolution of 5 µm. The power in the sample arm was 10 mW and the samples were imaged with a 40 mm lens producing a transverse resolution of 16 µm. The experiments for manual scanning at a larger scan range ~ 1 cm were conducted at a line scan rate of 1 kHz and an exposure time of 200 µs for the line scan camera. The other remaining experiments were performed at a line scan rate of 5 kHz. The sensitivity of the system at 1 kHz was measured to be 96 dB. The relatively low scan rate was chosen to allow sufficient time for manually translating the sample under the fixed OCT beam. The computer-controlled translational stage axes were aligned with the axes of a manually movable spring-loaded translational stage in order to obtain OCT images of the same cross-sectional planes within a sample while employing two different scanning mechanisms.

3. Results

3.1 Decorrelation curves for tissue phantoms and biological tissue

Figure 2(a) shows average decorrelation curves for several tissue phantom samples and biological tissues. The cross-correlation coefficients were obtained by an ensemble average of 400 A-scans at each lateral displacement. It was seen that there exists some degree of variability in the coefficients at each lateral position and this variability increases with an increase in the lateral displacement. Despite this variability, in general, the correlation coefficient values tend to decrease with increasing lateral separation. Except for the adipose sample, all samples exhibited a characteristic decorrelation length measured by the decrease in the cross-correlation coefficient to 1/e of their maximum value. This decorrelation length is approximately equal to the lateral resolution of the system, which governs the lateral speckle size in OCT images of scattering tissues [31]. The decorrelation length may be higher in samples containing prominent structural features as is evident in the case of adipose tissue which contains highly regular structural features typical of adipose cells. The preprocessing steps (moving average filter size and the A-scan truncation range) may also cause variations in the decorrelation lengths between different samples as the correlation coefficients may be influenced by the contributions of noise and the varying beam diameter within the truncated A-scans. All the decorrelation curves converge to a low correlation value for a lateral displacement well beyond the transverse resolution of the system.
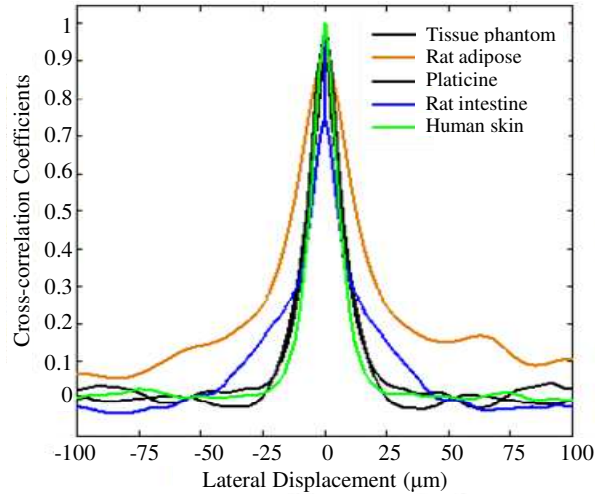
Fig. 2. Decorrelation curves obtained from galvanometer-scanned images of several tissue phantom samples and biological tissues (negative distance corresponds to the cross-correlation between the current A-scan and previously acquired A-scans). The tissue phantom was a silicone-based sample with titanium dioxide (TiO_2) scattering particles.

3.2 Image assembly for a tissue phantom

For proof-of-principle, a silicone-based tissue phantom was created with titanium dioxide (TiO_2) scattering particles (size < 5 µm). A standard galvanometer-scanned OCT image of the phantom was acquired. The means and the standard deviations of the cross-correlation coefficients for over 2000 A-scans at different lateral displacements were computed and are shown in Fig. 3(a). The OCT beam was then held fixed while the sample was moved along the lateral direction with 5 different velocities using a computer-controlled movable stage. A threshold of 0.8 corresponding to a sampling factor of 4 was selected from the decorrelation curve. The images were then downsampled using the algorithm for the chosen sampling factor. The higher the velocity, the lower the sampling factor would be, and a lesser number of A-scans would be selected per resolution element. We define a new parameter for the downsampled image assembled by our algorithm, A-scan redundancy ratio (ARR), as the number of A-scans compared for each selected A-scan. The mean and the standard deviation of the A-scan redundancy ratio (ARR) are shown in the blue curve in Fig. 3(b).
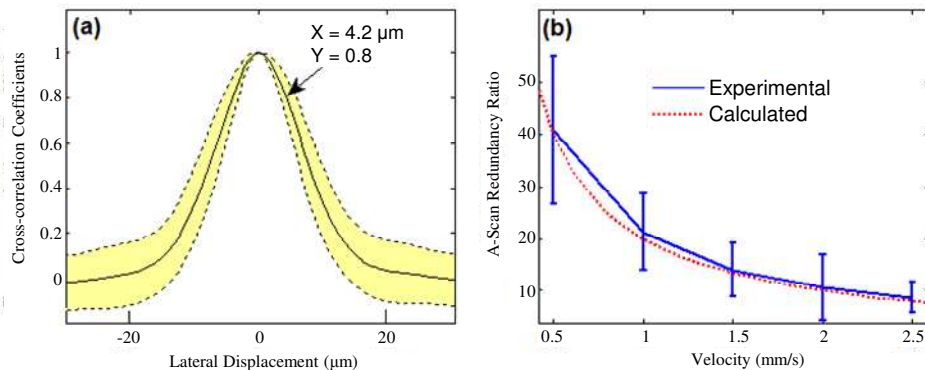

Fig. 3. Results with a silicone-based tissue phantom with titanium dioxide (TiO_2) scattering particles. (a) Decorrelation curve as a function of lateral distance. The solid curve is the mean and the dotted curves are the standard deviations of the correlation coefficients. (b) A-scan Redundancy Ratio (ARR) as computed by the algorithm for various sample scan velocities. The error bars show one standard deviation above and below the mean.

Equation. (1) was used to calculate the actual sampling factor for different scan velocities given the A-scan rate of 5 kHz and transverse resolution of 16 µm. The calculated sampling factor was then divided by the desired sampling factor (equal to 4 in this case) to calculate the ARR between the raw and assembled image and is plotted as the red dotted curve in Fig. 3(b). The results show that the experimentally-obtained results are in good agreement with the numerically-predicted values. The algorithm is able to compensate for variations in scan velocity by adjusting the periodicity of A-scan selection from the raw image data set. As seen in Fig. 3(b), the ARR curve is more sensitive to velocity variations for highly oversampled datasets, suggesting that the algorithm will provide better results for raw images taken with higher sampling factors. This would occur with slower scanning velocities or with advanced OCT systems with exceptionally fast A-scan acquisition rates.

Figure 4 shows image assembly with a non-uniformly scanned tissue phantom. All images have been log-normalized and displayed in the inverted gray scale. Figure 4(a) shows the tissue phantom uniformly sampled in time and distance. Figure 4(b) constitutes 5000 A-scans acquired over duration of 5 seconds by non-uniform scan velocity of the sample. The OCT beam was held fixed and the phantom was translated along the lateral direction with a motorized stage. Approximately 1900 A-scans were acquired while the sample moved at a velocity of 2.5 mm/s and 0.5 mm/sec, respectively, and roughly 1200 A-scans were acquired during the stop interval in between.
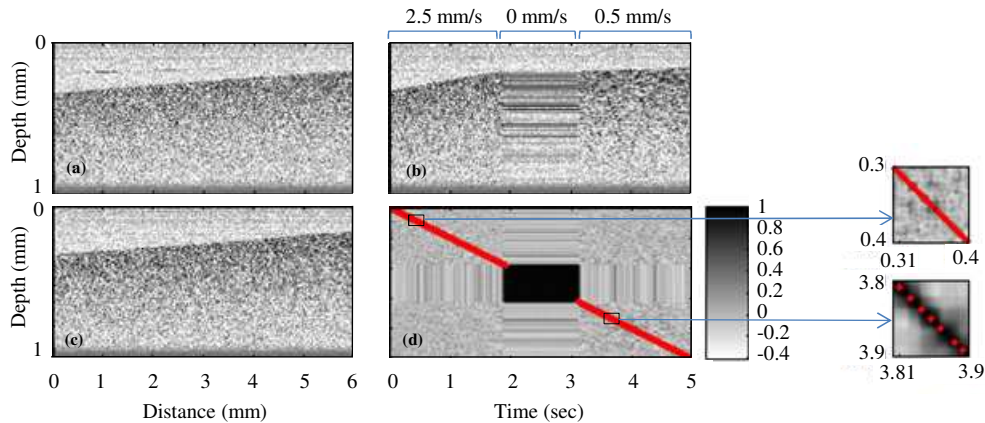

Fig. 4. Image assembly for a silicone-based tissue phantom with titanium dioxide (TiO_2) scattering particles. (a) Motorized stage scanned image (uniformly sampled in distance and time). (b) Non-uniformly scanned image (sampled non-uniformly in distance but uniformly in time). (c) Assembled image using A-scan selection algorithm (compensated for non-uniform sampling in distance). (d) Cross-correlation matrix with red points showing the A-scans selected for image assembly by the algorithm.

To aid visualization of the A-scan selection process from the algorithm, the correlation matrix is displayed in the form of a 2-D image (Fig. 4(d)). Each row shows the variation of the cross-correlation coefficients as a function of the adjacent A-scans. A solid diagonal line would correspond to the fact that the A-scans are perfectly correlated with themselves. The red points show the A-scans selected by the algorithm for assembling the image. The spacing of these red points will vary depending on the degree of sampling of the A-scans. In a relatively homogeneous sample, as shown in Fig. 4, the spacing of the red points varied proportionally with the degree of sampling. The zoomed-in areas show the different ARR corresponding to different sample scan velocities. It should be noted that calculating the complete cross-correlation matrix is not necessary for image assembly. Rather it is merely shown here to aid in visualizing the variations of cross-correlation coefficients with lateral

displacement, where dark regions correspond to little or no movement and lighter regions correspond to rapid movements.

Figure 4(c) shows the result after correcting for non-uniform sampling in distance. A threshold value of 0.7 was used for image assembly corresponding to a sampling factor of 2. The algorithm selected approximately 580 and 135 A-scans from the regions corresponding to the velocities 2.5 mm/sec and 0.5 mm/sec, respectively, making the assembled image uniformly sampled with a sampling factor of 1.95-2.30.

Figure 5 shows the result from manually scanning a spring loaded guide stage upon which a plasticine sample was mounted, over a distance of 1 cm. Plasticine is a highly scattering medium with limited penetration depth. The surface features were placed in the sample by manually scratching and carving the surface with a razor blade. The algorithm is able to assemble most of the surface image features using a threshold value of 0.3. The average sampling factor in Fig. 5(b) is estimated to be 4. The assembled image in Fig. 5(c) consists of ~ 600 A-scans. The algorithm fails near the 4 mm mark in Fig. 5(a) due to the highly similar surface features which are misinterpreted as stops by the algorithm.
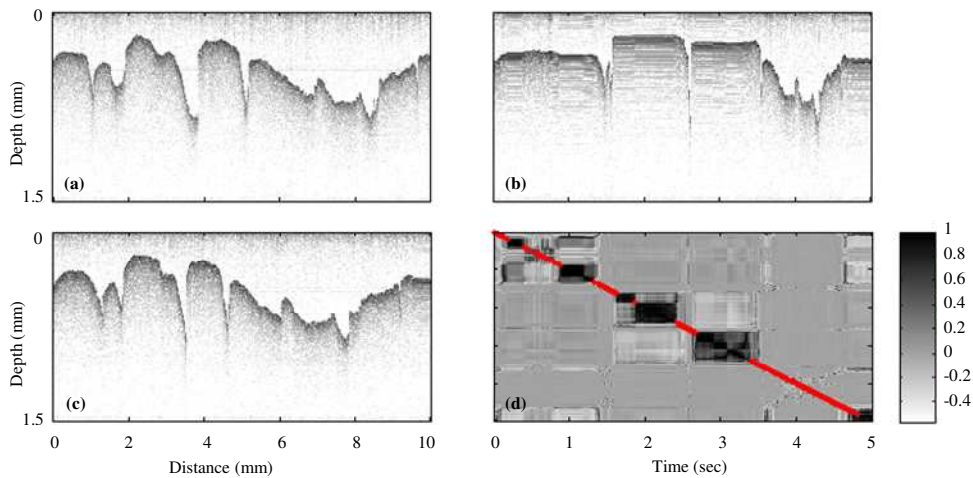

Fig. 5. Image assembly for a plasticine sample over a sample length of 1 cm. (a) Uniformly scanned image using a motorized stage. (b) Non-uniform hand-scanned image. (c) Assembled image. (d) Cross-correlation matrix with red points showing the A-scans selected for image assembly.

3.3 Image assembly for biological tissues

The human tissue used in this study was acquired and handled under a protocol approved by the Institutional Review Boards at the University of Illinois at Urbana-Champaign and Carle Foundation Hospital (Urbana, IL). The images of these biological tissues appear noisy because the SNR of the OCT system was kept suboptimal (around 93 dB) to validate this technique for images with relatively low SNR. In Fig. 6, human adipose tissue resting on the spring loaded guide stage, was manually scanned over a distance of 1.5 mm. A threshold value of 0.7 was used due to the relatively slow rate of decorrelation of adipose tissue. A line scan rate of 5 kHz was used for A-scan acquisitions. The assembled image in Fig. 6(c) has good correlation with the galvanometer scanned image in Fig. 6(a). Limitations in the algorithm are apparent at the lateral displacement of 0.3-0.5 mm in Fig. 6(c) which are believed to be due to hand vibrations while trying to hold the spring-loaded stage still. These vibrations cause rapid decorrelation of the A-scans which the algorithm misinterprets as valid probe displacements.
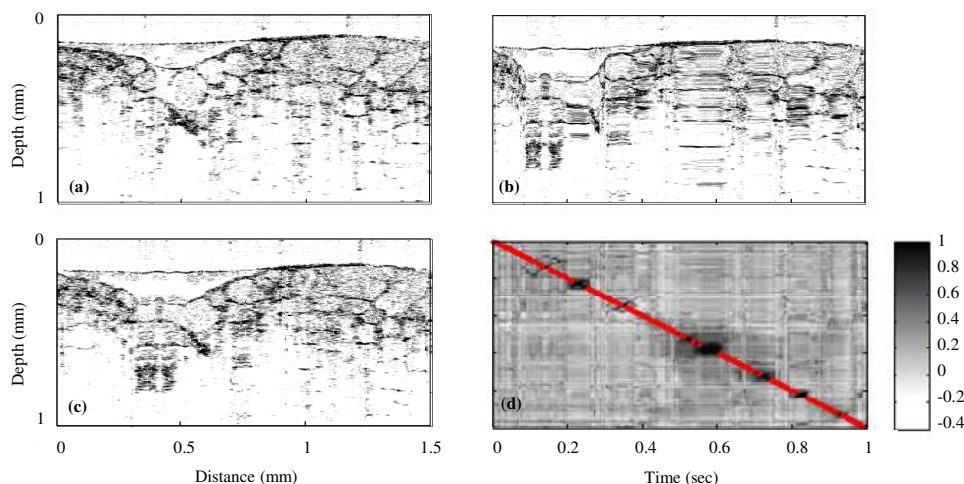
Fig. 6. Image assembly for human adipose tissue over a sample length of 1.5 mm. (a) Galvanometer-scanned image. (b) Non-uniform hand-scanned image. (c) Assembled image. (d) Cross-correlation matrix with red points showing the A-scans selected for image assembly.

Figure 7 shows the results with manual free-hand scanning of human breast tissue containing both tumor and adipose tissues. The sample was moved manually under a fixed OCT beam along a distance of 1 cm. The sample was stopped for various lengths of time during scanning as shown in Fig. 7(b). The assembled image in Fig. 7(c) shows that the algorithm is able to remove the artifacts associated with abrupt stops during manual scanning. The differences between the motorized-stage scanned image and the hand-scanned image are likely due to the misalignment of the scanning plane since the sample was manually scanned by free-hand, i.e. without the translational axis being guided by the spring loaded stage.
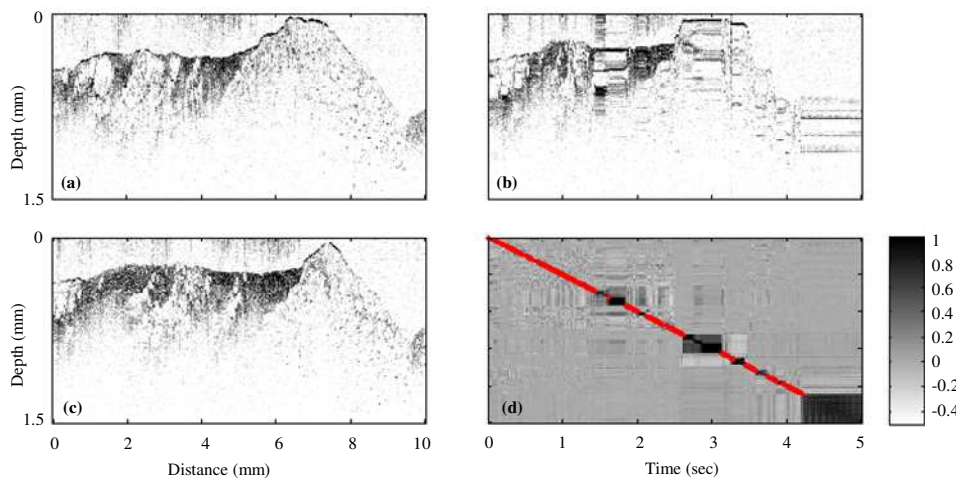

Fig. 7. Image assembly for a human breast tissue over a sample length of 1 cm. (a) Uniformly scanned image using a motorized stage. (b) Non-uniform hand-scanned image. (c) Assembled image. (d) Cross-correlation matrix with red points showing the A-scans selected for image assembly.

4. Discussion

A novel technique for image formation with sensor-less manual scanning of the sample has been described in this study. Although successful image assembly was demonstrated for a

range of phantom samples and biological tissues, there are certain limitations that need to be accounted for when performing real-time *in vivo* imaging. In this section, we present a discussion on applicability, limitations, and scope of further improvements in this image assembly technique.

In order to ensure image assembly while minimizing distortions and inaccuracies, the decorrelation curves need to be carefully calibrated with the lateral displacement. Selecting the right threshold is important for accurate image assembly. The current selection method was based on the decorrelation curves of the particular sample. Plots similar to those shown in Fig. 3(a) were used to select the optimal threshold for displacement separation. This technique will work best in highly scattering tissues where decorrelation lengths, governed by the speckle size, are given by the lateral resolution of the system. The results show that there exist inter-sample and intra-sample variations in the correlation coefficients at each lateral displacement. These variations can be attributed to inhomogeneity of structural features in tissues, variability in speckle patterns, and noise in the system.

However, the results can be significantly improved by adaptively modifying the threshold value to make the decorrelation curves less sensitive to the changing image features. This suggests that it would be beneficial to utilize real-time tissue classification algorithms to adaptively adjust the threshold value [33]. Further experiments also need to be done to investigate the dependency of various parameters on the decorrelation curves. It is also to be noted that the decorrelation curves decay down to a small cross-correlation coefficient value beyond the transverse resolution of the system. A lower threshold based on this value can provide accurately spaced images, but at the expense of a lower sampling factor and associated degradation in image quality.

This technique may impose certain limitations on the speed of image acquisition. Our experimental results show that a sampling factor as high as ~ 50 may be necessary for good results. Hence the velocity of the probe has to be constrained so that the sample is sufficiently oversampled. However, this limitation could be easily countered due to the availability of high-speed OCT systems [4, 34]. While commercial OCT systems have scan rates in the range of 25-40 kHz, fast swept-source or spectrometer-based OCT systems can extend the A-scan rates to several hundreds of kHz. For instance, a typical Fourier-domain OCT system with a 25 kHz A-scan rate may allow a probe with 16 µm lateral resolution to be moved with a maximum velocity of 8 mm/s while still allowing a sampling factor of 50. Hence fast OCT systems would allow reasonable freedom to allow free-hand manual scanning without compromising the effectiveness of the algorithm. An attractive feature of this technique is the relative computational and numerical simplicity which can enable image acquisition to be done in real-time.

Changes in scanning direction or variation in the angular orientation of the beam will cause misrepresentation of the images in the current algorithm, when compared to the galvanometer-based scanning that occurs in a single well-defined two-dimensional plane. The present algorithm only attempts to assemble images of samples moved in a lateral plane, but by selecting depth-dependent regions along each A-scan from which to do cross-correlations between adjacent A-scan regions, it may be possible to track angular out-of-plane displacements as well. The intended application for this approach is to assemble large images over scan ranges that exceed the capabilities of current galvanometers and computer-controlled scanning techniques. In cases for a hand-held probe, needle-probe, or catheter, the precise in-plane orientation of the acquired data may not be as critical as it is to capture adjacent A-scans over large lateral distances. Motion artifacts due to hand vibrations or jitter are more difficult to compensate because the technique is not sensitive to direction of displacement between A-scans. In our experiments these artifacts arise due to slight jitter of the hand while trying to hold the manually movable spring-loaded translational stage still. In the cross-correlation matrix these artifacts appear as varying coefficients with relatively low value. More sophisticated algorithms can be designed to compensate for these effects. Cross-

correlating a block of A-scans rather than single A-scans can potentially be used to detect change in scan direction and orientation of the probe [35]. Undersampling can be detected by comparing the cross-correlation coefficients of adjacent A-scans against a lower threshold value. Subsequently, interpolation algorithms can be used to estimate the missing A-scans [36].

Further, this technique can be combined with various other methods for motion estimation. In particular, extracting phase to detect precise motion seems to be a promising advancement. However, in our studies, the rapid variability of phase between adjacent A-scans made it an unreliable metric for quantifying the amount of lateral displacement. A more realistic approach towards manual scanning could be the use of this technique in tandem with external sensor based position tracking methods to estimate the direction and orientation of the probe. High resolution achievable by this technique can potentially be utilized to improve the accuracy of sensor-based position tracking methods which typically have sub-millimeter resolution.

5. Conclusions

In summary, we have described a novel cross-correlation based approach for image acquisition utilizing the structural and speckle information from the acquired A-scans. We demonstrate successful implementation of this technique to assemble manually-scanned images of several phantom samples and biological tissues. The algorithm may be used to perform semi-automatic real-time image acquisition. Adjustments of the parameters, in particular the decorrelation threshold, may be required depending on the structure and scattering properties of the biological tissue. The use of real-time tissue classification algorithms could be utilized to enhance the performance of the algorithm by adaptively adjusting this threshold.

This method can significantly enhance OCT capabilities for imaging over an extended field-of-view in an inexpensive way with user-defined scan geometry. In addition to the extended scan range, this algorithm can be adapted to obtain images at a deeper penetration depth by using needle-based OCT imaging systems. The method may also be adapted for use with a 2D mechanically-scanned handheld probe to provide 3D imaging over a large lateral field-of-view. Overall, this technique presents an attractive, simple, and cost-effective alternative to conventional galvanometer- or stage-based scanning and could contribute significantly towards intraoperative or intraprocedure OCT imaging applications.

Acknowledgments